UC Santa Cruz
UC Santa Cruz Previously Published Works

Authors

Filardi, Leah R
Yang, Feipeng
Guo, Jinghua
et al.

PCCP

PAPER

Check for updates

Surface basicity controls C–C coupling rates during carbon dioxide-assisted methane coupling over bifunctional Ca/ZnO catalysts†

Leah R. Filardi, [iD] [a] Feipeng Yang, [iD] [b] Jinghua Guo, [iD] [b] Coleman X. Kronawitter [iD] *[a] and Ron C. Runnebaum [iD] *[ac]

Carbon dioxide-assisted coupling of methane offers an approach to chemically upgrade two greenhouse gases and components of natural gas to produce ethylene and syngas. Prior research on this reaction has concentrated efforts on catalyst discovery, which has indicated that composites comprised of both reducible and basic oxides are especially promising. There is a need for detailed characterization of these bifunctional oxide systems to provide a more fundamental understanding of the active sites and their roles in the reaction. We studied the dependence of physical and electronic properties of Ca-modified ZnO materials on Ca content *via* X-ray photoelectron and absorption spectroscopies, electron microscopy, and infrared spectroscopic temperature-programmed desorption (IR-TPD). It was found that introduction of only 0.6 mol% Ca onto a ZnO surface is necessary to induce significant improvement in the catalytic production of C_2 species: C_2 selectivity increases from 5% on un-modified ZnO to 58%, at similar conversions. Evidence presented shows that this selectivity increase results from the formation of an interface between the basic CaO and reducible ZnO phases. The basicity of these interface sites correlates directly with catalytic activity over a wide composition range, and this relationship indicates that moderate CO_2 adsorption strength is optimal for CH_4 coupling. These results demonstrate, for the first time to our knowledge, a volcano-type relationship between CO_2-assisted CH_4 coupling activity and catalyst surface basicity, which can inform further catalyst development.

1. Introduction

Methane is the dominant constituent of natural gas, biogas, and shale gas, and due to advances in extraction and production technologies, it is an abundant resource.[1] However, the lack of technology to chemically utilize this resource efficiently leads to the practice of methane flaring and, thus, greenhouse gas emissions. There is a resurgent interest in pursuing the oxidative coupling of methane (OCM) as a viable avenue for methane upgrading into larger hydrocarbons.[2] However, when O_2 is used as an oxidant, product selectivity is hindered by over-oxidation of methane and C_2 products to CO_x, which limits overall C_2 yield.[3] It has been demonstrated that carbon dioxide

is an effective soft oxidant, facilitating the conversion of primary greenhouse gases into both valuable C_2 products and syngas.[4,5]

In 1988, carbon dioxide was first introduced during oxidative coupling of methane with oxygen.[6] A promotional effect of CO_2 on C_2 yield, as well as the formation of C_2 products from reaction of methane and CO_2 in the absence of O_2 was observed. Since then, it has been shown for many metal oxide catalyst systems[7] that the presence of CO_2 alone in methane reactor feeds (that is, in the absence of O_2) facilitates C–C coupling (following convention, abbreviated in this article as CO_2-assisted oxidative methane coupling, or CO_2-OCM). Enhanced activity and selectivity have been demonstrated with binary metal oxide composites, specifically those comprised of a basic oxide and a reducible oxide, including CaO/CeO_2,[8] Sr/MnO,[9] and Ca/CrO_2.[10] It is proposed that the basic oxide promotes CO_2 adsorption, which undergoes dissociation at a site associated with the reducible oxide to form an active surface oxygen species.[11] This species can facilitate methane activation to generate methyl radicals, which are known to couple in the gas phase to form ethane and ethylene.[12]

The synergy between basic and reducible oxides was demonstrated by Wang and Ohtsuka using CaO/ZnO.[13] Pure CaO

a Department of Chemical Engineering, University of California Davis, Davis, CA 95616, USA. E-mail: ckrona@ucdavis.edu, rcrunnebaum@ucdavis.edu

b Advanced Light Source, Lawrence Berkeley Nation Laboratory, Berkeley, CA 94720, USA

c Department of Viticulture and Enology, University of California Davis, Davis, CA 95616, USA

† Electronic supplementary information (ESI) available: Additional characterization results including BET, SEM, STEM, XPS, XANES, and IR-TPD with CO_2 flow. See DOI: https://doi.org/10.1039/d3cp00332a

This journal is © the Owner Societies 2023

Phys. Chem. Chem. Phys., 2023, **25**, 9859–9867 | 9859

catalyzes CO_2-OCM with moderate selectivity but very low yield, while pure ZnO preferentially forms syngas *via* methane reforming. When compared to the pure oxide components, the composite materials yield enhanced activity and selectivity, reaching 80% selectivity to C_2 products. However, it was shown that varying Ca composition from 10 to 50 mol% results in very similar catalyst performances, implying there is little change in the active site structure over this wide composition range.[13] The absence of significant influence of composition on catalyst performance has been reported for several other binary oxides containing either CaO[10,14] or ZnO.[11,15] For CO_2-OCM, there has been a dominant focus on catalyst discovery, which has precluded a much-needed detailed investigation of these promising bifunctional oxide systems. Thus, a fundamental understanding of the active sites and their roles in the reaction is lacking.

In the present work, we combine a suite of complementary characterization techniques, including most notably infrared spectroscopic temperature programmed desorption (IR-TPD), to understand the composition dependence of properties of a model binary Ca/ZnO catalyst at Ca levels much lower than those previously reported. Studying catalysts with very low concentrations of the basic oxide reveals information on the formation of the sites responsible for the promoted coupling activity. We herein demonstrate that the interface sites between the two metal oxides are critical to methane activation and selective coupling, which is attributable to their optimal moderate basicity. Throughout this article, we use the notation Ca/ZnO to refer to Ca-surface-loaded ZnO catalyst samples, but surface Ca–O species are described as oxides for convenience, since Ca is oxidized in all conditions examined.

2. Experimental methods

2.1. Catalyst synthesis

Ca/ZnO catalysts were prepared *via* a wet impregnation synthesis published previously by Wang and Ohtsuka.[13] The calculated amount of calcium nitrate tetrahydrate (99% ACS Reagent, MP Biomedicals) to provide the desired Ca/(Ca + Zn) composition (indicated as mol% in this article) was dissolved in MilliQ (18 Mohm) water (5 mL g^{-1} ZnO). Zinc oxide (99.9% metal basis, Alfa Aesar) was added, and the resulting slurry was sonicated to maximize ZnO dispersion in the solution. The mixture was partially covered and stirred at room temperature overnight until the water evaporated. The resulting white solids were then dried in an oven at 120 °C for 24 hours before calcining in 50 mL min^{-1} air (zero air, Praxair) at 850 °C (ramp 5 °C min^{-1}) for 4 h. Calcium oxide was synthesized by heating 100 mL of a 0.25 M calcium nitrate solution in an oil bath to 80 °C.[16] Under vigorous stirring, a 50 mL solution of 1 M NaOH was added dropwise, resulting in a cloudy solution of white precipitate. The solids were vacuum filtered, washed with MilliQ water, and dried overnight at 120 °C before calcination (see above).

2.2. Catalytic activity measurements

CO_2-OCM was conducted in a quartz down-flow, packed-bed reactor with 4 mm ID. A sample mass of 100 mg was loaded into the tube, supported by quartz wool (Acros Organics). The reactor was heated in a tubular furnace at 8 °C min^{-1} to 850 °C under 13.3 mL min^{-1} nitrogen (99.999%, Praxair). Flow was then switched to bypass the reactor and adjusted to 3.3 mL min^{-1} methane ($\geq$ 99.999%, Airgas), 6.7 mL min^{-1} carbon dioxide (pure clean grade, Airgas), and 3.3 mL min^{-1} nitrogen prior to flow through the reactor. Reaction products were measured by an online Agilent 7890A gas chromatograph (GC) with a FID and TCD. Empty reactors were used to determine conversion in the absence of catalyst prior to each experiment. This conversion was subtracted from the catalysis results. Relevant reaction parameters are defined as follows:

$$C_2 \text{ selectivity } \% = \frac{2\dot{n}_{C_2H_x}}{\dot{n}_{C,\text{prod}}} \times 100\%$$

$$\text{Conversion} \% = \frac{2\dot{n}_{C_2H_x} + \dot{n}_{CO,\text{reform}}}{\dot{n}_{i,\text{react}}} \times 100\%$$

where $\dot{n}_{C_2H_x}$ is the molar flowrate of C_2 products, $\dot{n}_{C,\text{prod}}$ is the molar flowrate of all carbon atoms in products, $\dot{n}_{i,\text{react}}$ is the initial molar flowrate of the reactant of interest, and $\dot{n}_{CO,\text{reform}}$ is the molar flowrate of CO originating from CH_4 in the reforming of CH_4, calculated by $(-\dot{n}_{C_2H_4} - \dot{n}_{C_2H_4} + \dot{n}_{H_2} + \dot{n}_{CO})/4$.[7]

C_2 yield is defined as the total molar flowrate of ethane and ethylene as measured by GC.

2.3. Materials characterization

Calcium loading was quantified by inductively coupled plasma mass spectrometry (ICP-MS) after acid digestion with an Agilent quadrupole mass spectrometer 7500. Nitrogen physisorption isotherms were measured using a Micromeritics 3Flex physisorption/chemisorption instrument. Physisorption measurements were made at −196 °C. Samples were degassed at 300 °C for 3 hours under vacuum prior to analysis. Surface areas were determined by the BET method. Scanning electron microscopy (SEM) was performed on a Thermo Fisher Scientific Quattro ESEM. Samples were pressed onto carbon tape on a sample stub. Images were acquired under vacuum using a spot size of 3 and an accelerating voltage of 5 kV. X-ray diffraction (XRD) patterns were recorded on a Bruker D8 Advanced Diffractometer with Cu Kα radiation. Powder samples were sieved through a 304 stainless steel wire cloth disc with a mesh size of 200 to ensure a random distribution of exposed facets. They were adhered to silica sample holders with Dow Corning high vacuum grease. For scanning transmission electron microscopy (STEM) analysis by a JEOL-JEM 2500SE electron microscope, dilute suspensions of samples were drop-cast on copper-supported lacey carbon grids and dried overnight. Energy dispersive X-ray spectroscopy (EDS) was performed using a Thermo Corporation EDS spectrometer attached to the JEOL JEM 2500SE. X-ray photoelectron spectroscopy (XPS) was performed using a Kratos AXIS Supra spectrometer equipped with a monochromatic Al Kα anode (1486.6 eV). Air-exposed powder samples were adhered to carbon tape and loaded into a flexi-

9860 | *Phys. Chem. Chem. Phys.*, 2023, **25**, 9859–9867

This journal is © the Owner Societies 2023

lock. The flexi-lock was pumped down to 10^{-7} torr before transfer of the samples to the analysis chamber. Binding energies were charge-corrected by aligning the Zn $2p_{3/2}$ peak to 1021.9 eV.[17] The data were processed and analyzed using Kratos ESCApe software. Synchrotron X-ray absorption spectroscopy (XAS) experiments of the Ca and Zn L-edge regions were conducted at beamline 7.3.1 of the Advanced Light Source (ALS), Lawrence Berkeley National Laboratory. Spectra of total electron yield (TEY) were collected and charge-corrected by referencing a standard of the metal oxide to known values.[18,19] Diffuse reflectance infrared Fourier transform spectroscopy (DRIFTS) was performed with a Bruker Tensor II FTIR Spectrometer equipped with a Pike Technologies DiffusIR MidIR Accessory. Spectra were collected with 128 scans at a resolution of 2 cm^{-1}. *In situ* calcinations were performed by heating the sample 10 °C min^{-1} to 850 °C for 30 minutes under 20 mL min^{-1} of dry air flow. Background spectra were collected at each temperature of interest under N$_2$ flow during the cooling ramp following the calcination. The cell was held at the target temperature for 5 minutes prior to collecting the background spectra. At room temperature (below 30 °C), CO$_2$ was introduced by flowing 2.5 mL min^{-1} of CO$_2$ with 47.5 mL min^{-1} of N$_2$ for 1 minute. Carbon dioxide was purged from the cell by cycling the cell between vacuum and N$_2$ refill 3 times followed by 20 mL min^{-1} N$_2$ flow for 1 hour. Temperature-programmed carbonate desorption was measured by heating the sample 1 °C min^{-1} to 800 °C under 20 mL min^{-1} of dry air flow and collecting spectra every 50 °C.

3. Results and discussion

3.1. Catalysis results

Ca/ZnO catalysts with various Ca surface loadings were synthesized *via* wet impregnation and evaluated for their CO$_2$-OCM performance (Fig. 1). At low loadings, introduction of Ca onto the ZnO surface drastically shifts the product distribution from syngas to C$_2$ hydrocarbon products. Increasing Ca loading increases C$_2$ selectivities until a maximum of 70.6% is reached. Most notably, increasing the Ca loading from 0.4 mol% to 0.6 mol% results in a 4-fold increase in C$_2$ selectivity and a 2-fold increase in the yield. Additions of Ca beyond 0.6% do not further improve the methane coupling yield, and at the highest loadings examined, addition of Ca decreases yields. Consistent with previous studies, pure ZnO preferentially generates syngas *via* methane dry reforming,[20] while pure CaO has little activity to both syngas and C$_2$ products. The low CaO activity has been attributed to low concentrations of defect sites,[21] which are understood to be essential to activation of methane. Ethane production is nearly double that of ethylene over all catalysts (Table S1 (ESI†) provides the measured product compositions for CO$_2$-OCM with all catalysts). While these results are consistent with early reports of enhanced coupling performance for binary metal oxides,[13] the impact of small amounts of added Ca (<1 mol%) in these experiments highlights its role in promoting CO$_2$ adsorption during reaction.
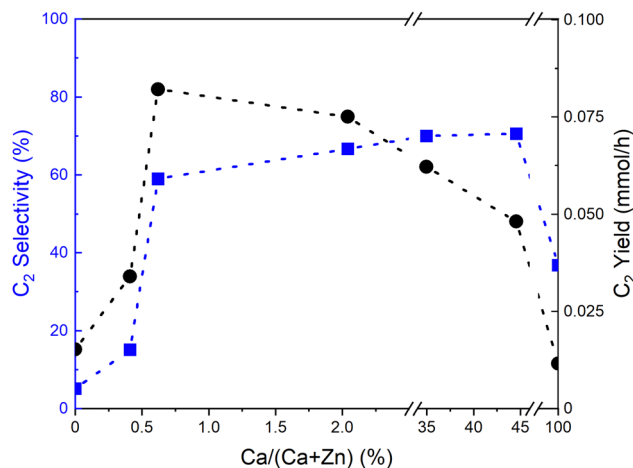

Fig. 1 Effects of Ca loading on C$_2$ selectivity (■) and C$_2$ yield (●). Reaction conditions: 850 °C; 100 mg catalyst; 13.3 mL min^{-1} total gas flow rate with P_{CH_4} = 0.25 atm, P_{CO_2} = 0.5 atm, P_{N_2} = 0.25 atm; 4 h on stream. Methane conversion was less than 7% (Table S1, ESI†). All Ca loadings are reported in molar concentration of metal cations, as determined by ICP-MS (Table S2, ESI†). Lines are included to guide the eye.

Motivated by work demonstrating a bifunctional mechanism for composite catalysts,[8–10] catalysis experiments with physical mixtures of pure CaO with ZnO were performed to investigate the role of the interface between Ca (or CaO) and ZnO in CH$_4$ coupling. Experiments in which the CaO was physically separated from ZnO by quartz wool, shown in Fig. 2, yield a product distribution almost identical to that from pure ZnO. This is consistent with the relative inactivity of pure CaO for CO$_2$-OCM catalysis. Physically mixing CaO with ZnO favors CH$_4$ reforming at short times-on-stream but C–C
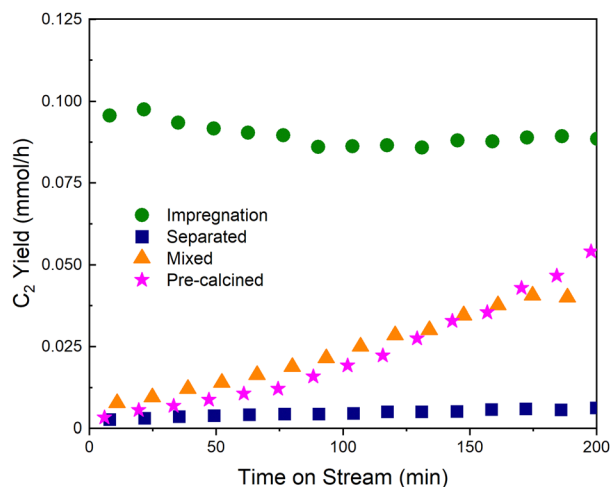

Fig. 2 Contrasting C$_2$ product yields associated with various methods of loading 0.6% Ca + ZnO into reactor on C$_2$ yield. Impregnation: ZnO impregnated with Ca salt (●); mixed: well-mixed physical mixture of CaO and ZnO (▲); pre-calcined: physical mixture of CaO and ZnO that was calcined to 850 °C in air prior to reaction (★); separated: loading that isolates upstream CaO from downstream ZnO with quartz wool (■). Reaction conditions: 850 °C; WHSV = 8.0 L h^{-1} g$_{cat}^{-1}$ with P_{CH_4} = 0.25 atm, P_{CO_2} = 0.5 atm, P_{N_2} = 0.25 atm.

This journal is © the Owner Societies 2023

Phys. Chem. Chem. Phys., 2023, **25**, 9859–9867 | **9861**

coupling activity increases with longer times-on-stream. This outcome could be due to the sintering of the two oxides under the reaction temperature of 850 °C to form the relevant Ca/ZnO interface. To explore this hypothesis further, a mixture of the two oxides were calcined in air at 850 °C before being loaded into the reactor; this configuration yielded results nearly identical to those from the non-calcined mixture. This result indicates that the active sites for selective CH_4 coupling are not formed by temperature-induced sintering in a highly oxidative environment (here, pure O_2 at elevated temperature). Therefore, the more reductive environment of the reaction mixture is likely the primary origin of modifications to catalyst surfaces with time on stream. Zinc oxide is known to easily form local oxygen vacancies under reducing conditions at high temperatures.[22–25] Under significantly reducing conditions, pure ZnO may also become partially reduced with metallic domains that can vaporize at reaction temperature, leading to some restructuring of the catalyst surface.[26] It is unlikely that CaO would also be reduced to any significant degree in these conditions. However, the CO_2 and water present under reaction conditions could promote CaO sintering.[27] Thus, the increased C_2 yield with longer time on stream is likely due to further interface formation, associated with oxygen vacancy generation as well as CaO sintering. Vacancies on ZnO are capable of dissociating CO_2,[28] and we propose in this report that those exposed to adsorbed CO_2 at neighboring Ca-containing sites are active for this reaction. The drastic differences in yields in reactor studies between Ca impregnation onto ZnO and physical mixtures of the constituent oxides suggest that the Ca–ZnO interface is critical for coupling to occur. The catalysts were further characterized to explain the trends in activity with Ca loading and to understand the role of the interface.

3.2. Catalyst characterization

BET measurements (Table S2, ESI†) reveal that pure CaO has $\sim$14 times higher surface area than pure ZnO. Surface areas of all Ca/ZnO samples are similar to those of pure ZnO. SEM images (Fig. S1, ESI†) indicate that there were no changes in ZnO bulk structure or morphology with increasing Ca concentration. Therefore, differences in activity are not correlated to surface area or morphology.

X-ray diffractograms, shown in Fig. 3a, reveal only the hexagonal ZnO phase (JCPDS 36-1451) and lack observable peaks corresponding to Ca species in samples with 0.6% Ca or less. No calcium zincate or complex oxide phase was observed. Within the resolution of our measurements, there is no indication in the diffractograms of modification to the ZnO lattice parameters. Increasing Ca concentration above 0.6% yields distinct bulk CaO phases. The sample with 2% Ca is characterized by minor peaks at 32.2°, 37.4°, and 53.9° (Fig. S2, ESI†), which are the dominant diffraction peaks for CaO. Long-range ordered CaO phases are only observed in samples with 2% and higher Ca content. The STEM image and EDX maps of the 35% Ca/ZnO sample in Fig. 3b–e show the existence of large CaO crystallites with length dimensions of hundreds of nanometers on the surface of ZnO particles. By

contrast, STEM images of the 0.6% Ca/ZnO sample do not show any visible CaO clusters (Fig. S3, ESI†). Lack of visible Ca species in these images is due to the low *Z*-contrast and high dispersion of Ca species at low loadings.

X-ray photoelectron spectra (XPS) of the Ca 2p region are shown in Fig. 3f. To account for binding energy changes due to charging, the energy scale was corrected using the Zn 2p peaks (Fig. S4c, ESI†) from the support; Ca loading is unlikely to modify the electronic structure of the support over the $\sim$10 nm probe depth of photoelectrons. The validity of this correction is confirmed by the consistency of the C 1s peak, which is commonly used for energy calibration (Fig. S4d, ESI†). The lack of influence of Ca on ZnO electronic structure is also confirmed for the high Ca-loading samples by Zn L_{23}-edge XANES (Fig. S5, ESI†). For these high Ca-loading samples, the Ca $2p_{3/2}$ and $2p_{1/2}$ peaks are observed at 347.6 and 351.2 eV, respectively.[17] The peaks shift to 348.0 and 351.6 eV for all samples with $\leq$2% Ca. The similar peak binding energies in the low-loading samples suggest that they contain similar Ca sites that are distinctly different from those in the high Ca-loading samples. The shift to higher binding energy for the low Ca-loading samples is consistent with support effects observed for supported metal oxide nanoparticles.[29,30] As CaO particle size grows, the Ca 2p binding energy approaches that of bulk CaO. Quantification of the fitted XPS peaks yields Ca concentrations well above the bulk concentrations as determined by ICP-MS (Table S2, ESI†). Given the surface sensitivity of XPS, it is clear that the Ca species are segregated at the surface of the ZnO particles, as illustrated by EDX mapping, rather than doped within the ZnO lattice. This is confirmed by the decrease in Ca intensity and corresponding increase in Zn intensity after argon etching the catalyst surface (Fig. S6, ESI†).

A trend across compositions is also observed in XANES spectra at the Ca L-edge, which is sensitive to the oxidation states and local environments of metals.[31] In these spectra, the peaks correspond to transitions from Ca 2p to primarily unoccupied Ca d states. Peaks in data from the low Ca-loading samples are shifted to a higher energy compared to those in the high Ca-loading samples (Fig. 3g), which is consistent with the XPS results. Taken together, the results from these characterization methods all support the conclusion that the Ca sites present in low concentrations are similar to each other, but distinct from those present in high concentrations, which is associated with large CaO crystallites.

The lack of long-range-ordered CaO phases in low-loading samples suggests the presence of a more dispersed state of Ca ions, and therefore a relative increase in the amount of interface sites containing Ca–O–Zn interactions. Fig. 2 illustrates the importance of the interface sites in CH_4 coupling, which we propose to be the most active sites for CO_2 and CH_4 dissociation. The effectiveness of each Ca atom in producing C_2 products is constant over low Ca concentrations (Fig. S7, ESI†), which suggests that the active site does not change with incremental addition of small amounts of Ca. The Ca-normalized C_2 product yield drastically declines from 167 to 75 mmol h^{-1} g_{Ca}^{-1} as loading is increased to 2% Ca, a state in

9862 | *Phys. Chem. Chem. Phys.*, 2023, **25**, 9859–9867

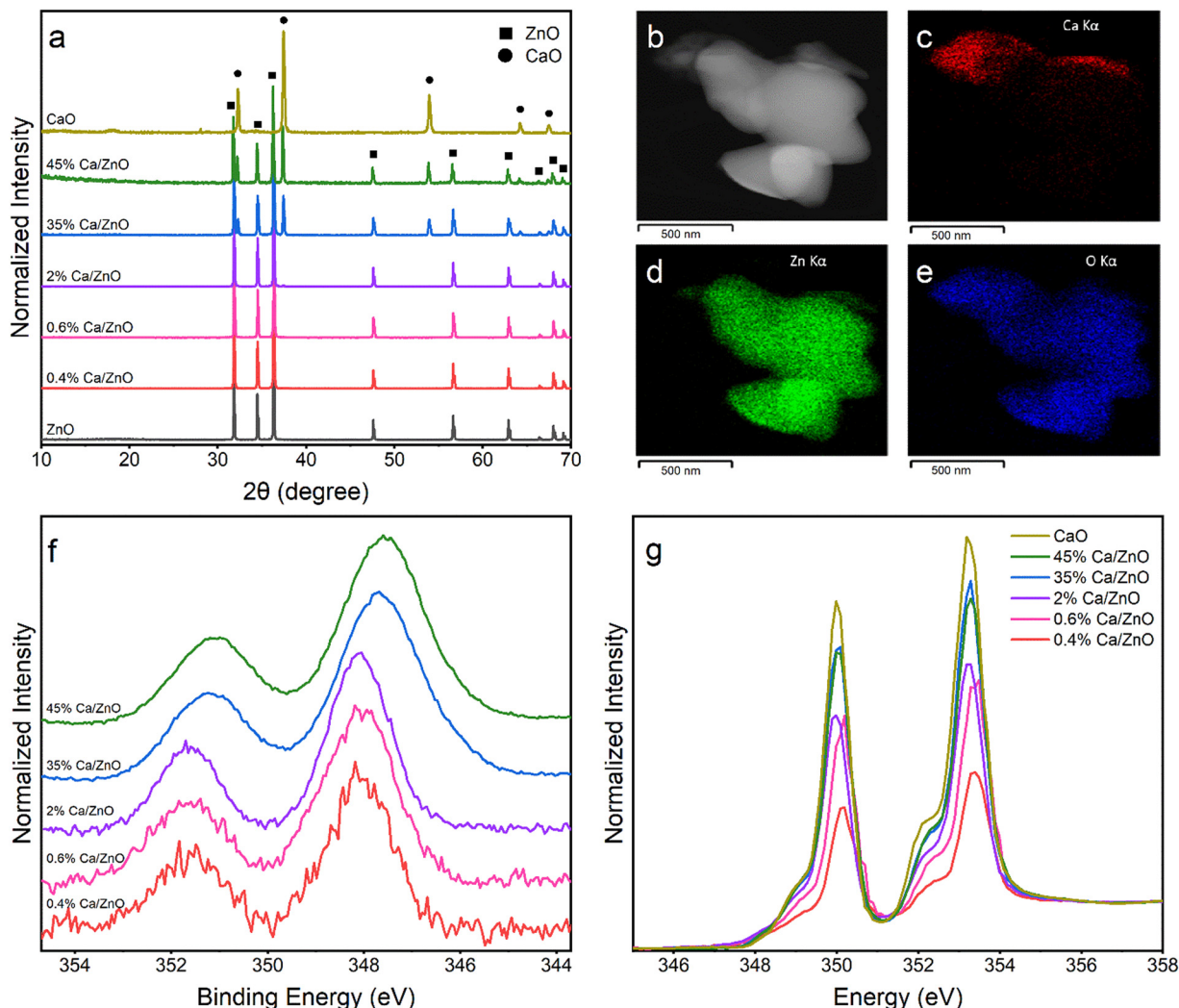This journal is © the Owner Societies 2023

Fig. 3 Physical and electronic characterization of the Ca/ZnO materials: (a) XRD patterns of calcined pure metal oxides and binary metal oxides with varied concentrations. (b) HAADF–STEM image of 35% Ca/ZnO, (c–e) EDX elemental mapping of Ca, Zn, and O, respectively. (f) XPS and (g) XANES spectra of Ca 2p region, which shows shifts to higher binding energies at lower Ca levels.

which the CaO bulk phase forms. It further decreases to 0.23 mmol h^{-1} g_{Ca}^{-1} for pure CaO. Therefore, the sharp increase in C_2 selectivity and yield with a very small increase in Ca concentration in Fig. 1 can be explained by an increase in the number of Ca atoms in close contact with the ZnO surface, creating interfacial active sites. The synergy between oxygen vacancy concentration and active site dispersion was reported to control oxygen abstraction rates in a mixed metal oxide catalyst,[32] emphasizing the role of interfaces in catalyst reactivity. We propose a similar mechanism of cooperation between oxygen vacancies and Ca-containing surface species. Thus, as Ca loading increases and dispersion decreases, C_2 product yield also decreases. The reaction data also suggest that Ca addition increasingly blocks or to some extent modifies ZnO sites responsible for methane reforming. Oxygen vacancies formed from reducible metal oxides can facilitate methane reforming.[33,34] However, neighboring Ca atoms may modify the structure and activity of these sites. Thus, the dominant reaction pathway

transitions from CH_4 reforming on the bare ZnO surface to coupling at the interfacial sites when surface Ca is introduced. Further addition of Ca leads to further enhancement of CH_4 coupling over reforming. The selective formation of ethylene *via* CO_2-OCM instead of CO *via* CH_4 dry reforming is highly dependent on whether CH_x species remain bound too strongly on the surface and undergo subsequent hydrogen abstraction.[35] More reducible catalyst surfaces adsorb CH_x species more strongly.[36] This explains the preferences for CH_4 dry reforming over ZnO catalysts. Loading another oxide onto the surface can suppress CH_4 reforming by decreasing the overall reducibility at the interface.[37]

To better understand the interaction of CO_2 with these material surfaces, CO_2 adsorption was studied with *in situ* DRIFTS experiments. After exposure to CO_2 at room temperature, prominent peaks are present around 1390–1560 cm^{-1}, 1630 cm^{-1}, 1772 cm^{-1}, and 2540 cm^{-1}, corresponding to unidentate carbonate, bicarbonate, bridging carbonate, and

This journal is © the Owner Societies 2023

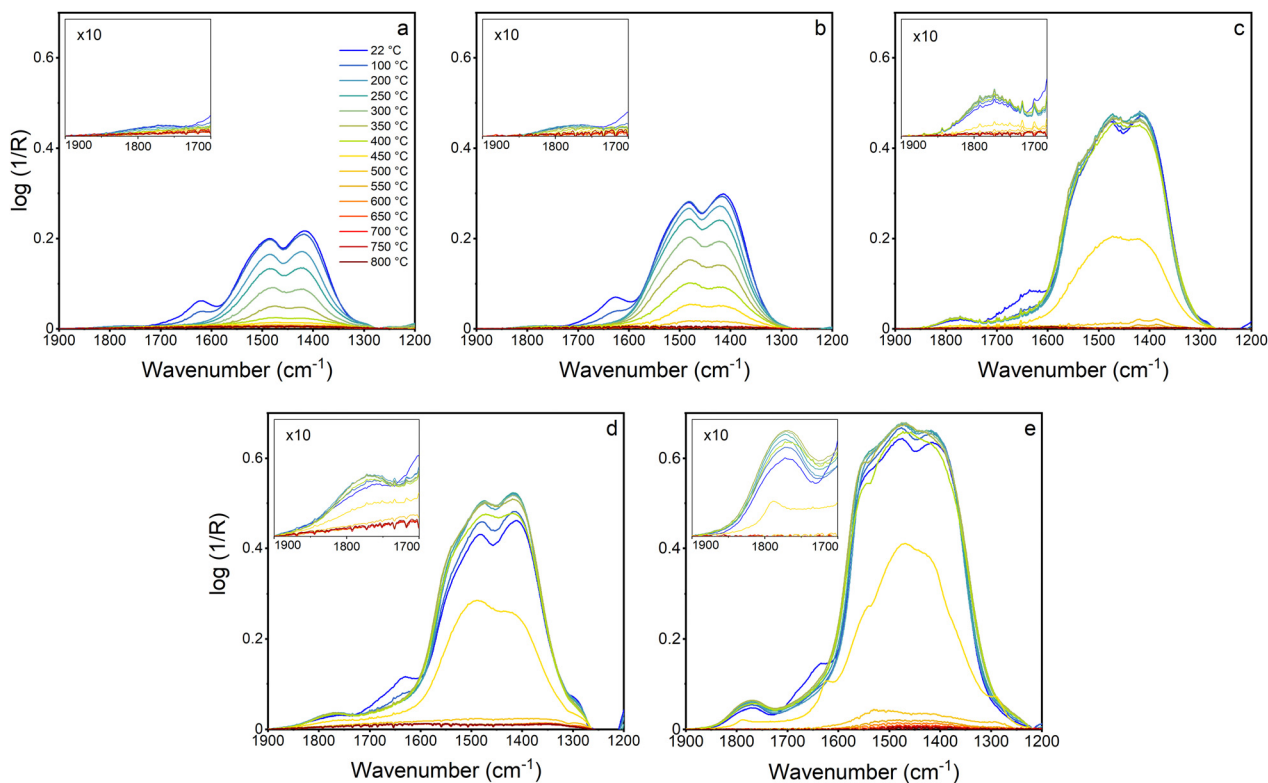*Phys. Chem. Chem. Phys.*, 2023, **25**, 9859–9867 | **9863**

Fig. 4 DRIFTS temperature-programmed desorption of carbonate on (a) 0.4% Ca/ZnO, (b) 2% Ca/ZnO, (c) 35% Ca/ZnO, (d) 45% Ca/ZnO, and (e) CaO after adsorption of CO_2 at room temperature, with temperature ramping in N_2 at rate 1 °C min^{-1}. Spectra have been subtracted by those of sample at corresponding temperature prior to carbonate adsorption. Desorption spectra for pure ZnO are shown in Fig. S8 in the ESI.†

linearly adsorbed CO_2 (Fig. 4), respectively.[38,39] Consistent peak positions are present in all Ca-containing samples and differ from those from CO_2 adsorption on pure ZnO (Fig. S8, ESI†). Even with low concentrations of Ca present, CO_2-surface interactions are limited to Ca-containing sites. Zinc oxide is known to poorly adsorb CO_2;[40] carbonate formation on ZnO is considered negligible. Unidentate carbonate is the most preferable mode of carbonate in all measured Ca-containing samples. The formation of bridging carbonates, shown in the insets of Fig. 4, requires at least two adjacent Ca atoms, and therefore the intensity of these peaks relates to the lack of Ca dispersion. Its presence in high Ca-loading samples with large CaO clusters is unsurprising. Bridging carbonate peaks are also present in the 0.4% Ca/ZnO, but with much lower intensity relative to the total carbonate concentration. This evidence supports the conclusion that most of the Ca-containing species are highly dispersed, likely existing as a mixture of mononuclear sites and nano-sized clusters. However, it is not possible to accurately identify either of these species without a measurement that is extremely sensitive to the location coordination environment of Ca, such as extended X-ray absorption fine structure (EXAFS).

After adsorption, the temperature-programmed desorption of the carbonate species in inert nitrogen atmosphere reveals that the catalysts with 2% or lower Ca content desorb carbonate at very low temperatures (less than 200 °C). The data also show

that carbonate is stable on the higher-Ca-loading samples up to 400 °C (Fig. S9a, ESI†); the carbonate stability on samples with CaO particles is consistent with the behavior of pure CaO.[38,41]

The desorption temperature of carbonates is a measure of oxide surface Brønsted basicity. In this system, evaluation of surface basicity informs not only on the nucleophilicity of the surface oxygen species but also how strongly CO_2, a reactant here, adsorbs and interacts with the catalyst surface. The rate-determining step of CO_2-OCM is thought to include CO_2 because of the reported relationship of C_2 product formation rate with the partial pressure of CO_2.[13,42,43] The rate of carbonate desorption can be approximated as a function of temperature.[44] The temperature at which the maximum rate of carbonate desorption is observed for each catalyst has been plotted against its activity (Fig. S9b, ESI†), which indicates a volcano-type relationship exists. This desorption temperature approximately tracks with Ca loading and therefore the activity trends with CO_2 desorption temperature shown in Fig. 5 closely resemble those in Fig. 1.

It is well-established that for a variety of reactions, including OCM,[45–47] CO_2 methanation,[48–50] methane dry reforming,[51–53] methanol carbonation,[54] and CO_2-assisted alkane dehydrogenation,[55] catalysts with medium-strength basic surface oxygen sites are optimized to increase activity. Strongly basic sites adsorb CO_2 strongly, which prevents turnover, and weakly basic sites are unable to efficiently adsorb and activate CO_2; medium-strength

9864 | *Phys. Chem. Chem. Phys.*, 2023, **25**, 9859–9867
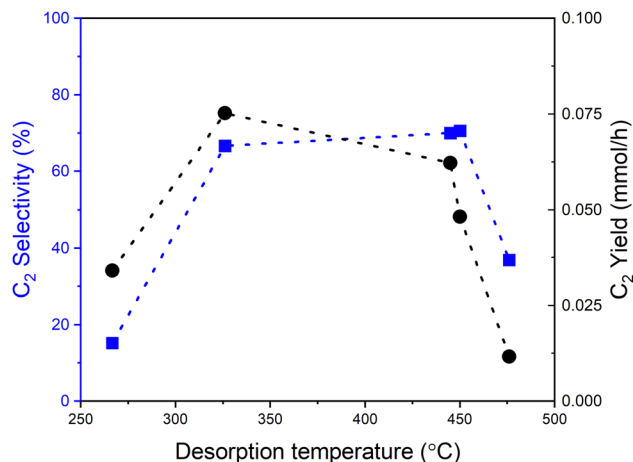
This journal is © the Owner Societies 2023

Fig. 5 Volcano relationship between catalyst performance and CO_2 desorption temperature indicating moderate basicity enhances C–C coupling performance. Lines are included to guide the eye.

sites provide a balance between these contrasting behaviors. For example, a prior study of OCM showed that a mixed metal oxide catalyst results in a defective structure with greater amounts of O_{vac} and medium-strength basic sites compared to both pure oxides.[46] The presence of these two sites in a single catalyst structure yields OCM activity greater than in the constituent pure oxides.

The basicity trends of the above examples likely result from the common involvement of the elementary step of oxygen dissociation from CO_2 in their mechanisms. Because the same trend can be observed here, we can infer a similar mechanism, which depends on the coexistence of O_{vac} and medium-strength basic sites, is operable for CO_2-OCM with this composite catalyst. Catalysts with primarily strong surface basic sites adsorb significant quantities of CO_2, which is associated with more stable carbonate under reaction conditions. These surface carbonates have been demonstrated to reduce yields of C_2 products with CaO catalysts because they block active sites.[21] Previous reports examining CO_2-OCM have shown that, when coupled with reducible oxide such as a ZnO or CeO_2, oxides more strongly basic than CaO such as SrO and BaO yield decreased CH_4 conversion and C_2 selectivity, with decreases associated with increasing basicity of the oxides.[9,14] Additional IR experiments performed in the presence of CO_2 show that in this condition carbonates remain on the catalyst surface at reaction temperature (Fig. S10, ESI†). In contrast, high concentrations of weakly basic sites both reduce the total amount of CO_2 on the catalyst surface and the rate of CO_2 dissociation, which is required to form reactive surface oxygen species. Istadi and Amin computationally determined that in a CaO-MnO/ CeO_2 catalyst, increasing CaO concentration up to 8.2 wt% enhances CO_2 adsorption and improves C_2 selectivity.[56] Calcium oxide is strongly basic and zinc oxide is weakly basic,[15,42] which is consistent with observations here on the low CH_4 coupling activity for both pure metal oxides. Using basicity as a tunable parameter to influence yield allows for flexibility in composition for catalyst design. In summary, the construction of a composite catalyst comprised of a strongly basic oxide and

weakly basic reducible oxide produces interfacial sites associated with moderate basicity, which enables C_2 product yields from CO_2-OCM greater than possible with the constituent oxides alone.

4. Conclusions

This work describes an investigation into the effects of Ca loading and associated electronic and physical properties to understand observed enhancements of CO_2-assisted CH_4 coupling with Ca/ZnO catalysts. Addition of a small amount – 0.6 mol% – of Ca to a ZnO catalyst surface was observed to result in a significant increase in both C_2 product selectivity and yield. Comparative reactor studies with physical mixtures of CaO and ZnO show that the presence of the interface between these oxides is essential for high coupling activity. The catalysts were characterized to understand this promotional effect and the role of the interface. XRD, XPS, and XANES results indicate that samples with less than 2 mol% Ca possessed characteristics distinct from those with greater amounts. IR-TPD was used to study surface basicity. Correlating these data with activity yields a volcano-type relationship between CO_2 adsorption strength on the catalyst surface and its performance as a catalyst for CO_2-assisted CH_4 coupling. Moderately basic sites are optimal for CH_4 coupling, which is consistent with results that have been reported for OCM with O_2 as the oxidant. All composite catalysts studied were associated with weaker CO_2 adsorption than pure CaO. Taken together, results from these characterization methods suggest that CH_4 coupling activity is controlled by the interaction of CO_2 at the interfacial sites between CaO and ZnO. The next steps of investigation of this system should involve work to characterize the interfacial sites using probes that are sensitive to the local chemical environment around metal centers, such as Ca and Zn K-edge EXAFS. These findings show that catalysts for CO_2-OCM can be designed to facilitate high C_2 product yields through optimization of basicity and concentration of sites that form at the interfaces between dissimilar metal oxides.

Author contributions

L. R. F. was responsible for project conceptualization, data acquisition and analysis, and manuscript writing. F. Y. and J. G. acquired and exported all XAS data. R. C. R. and C. X. K. contributed to project conceptualization and oversight, as well as manuscript review and editing.

Conflicts of interest

There are no conflicts of interest to declare.

Acknowledgements

This journal is © the Owner Societies 2023

Phys. Chem. Chem. Phys., 2023, **25**, 9859–9867 | **9865**

References

1 D. Hu, V. V. Ordomsky and A. Y. Khodakov, *Appl. Catal., B*, 2021, **286**, 119913.

2 R. Horn and R. Schlögl, *Catal. Lett.*, 2015, **145**, 23–39.

3 J. S. Lee and S. T. Oyama, *Catal. Rev.*, 1988, **30**, 249–280.

4 A. M. Arinaga, M. C. Ziegelski and T. J. Marks, *Angew. Chem., Int. Ed.*, 2021, **60**, 10502–10515.

5 X. Cai and Y. H. Hu, *Energy Sci. Eng.*, 2019, **7**, 4–29.

6 K.-I. Aika and T. Nishiyama, *J. Chem. Soc., Chem. Commun.*, 1988, 70–71.

7 K. Asami, T. Fujita, K.-I. Kusakabe, Y. Nishiyama and Y. Ohtsuka, *Appl. Catal., A*, 1995, **126**, 245–255.

8 Y. Wang, Y. Takahashi and Y. Ohtsuka, *Appl. Catal., A*, 1998, **172**, L203–L206.

9 Y. Wang and Y. Ohtsuka, *Appl. Catal., A*, 2001, **219**, 183–193.

10 Y. Wang, Y. Takahashi and Y. Ohtsuka, *Chem. Lett.*, 1998, 1209–1210.

11 C. Chen, Y. Xu, G. Li and X. Guo, *Catal. Lett.*, 1996, **42**, 149–153.

12 D. J. Driscoll, W. Martir, J.-X. Wang and J. H. Lunsford, *J. Am. Chem. Soc.*, 1985, **107**, 58–63.

13 Y. Wang and Y. Ohtsuka, *J. Catal.*, 2000, **192**, 252–255.

14 Y. Wang, Y. Takahashi and Y. Ohtsuka, *J. Catal.*, 1999, **186**, 160–168.

15 Y. He, B. Yang and G. Cheng, *Catal. Today*, 2004, **98**, 595–600.

16 Z. Mirghiasi, F. Bakhtiari, E. Darezereshki and E. Esmaeilzadeh, *J. Ind. Eng. Chem.*, 2014, **20**, 113–117.

17 J. F. Moulder, W. F. Stickle, P. E. Sobol and K. D. Bomben, *Handbook of X-ray Photoelectron Spectroscopy*, Perkin-Elmer Corporation, Eden Prairie, MN, 2nd edn, 1992.

18 M. Patel and P. B. Aswath, *Tribol. Int.*, 2012, **52**, 17–28.

19 M. Yuste, R. Escobar Galindo, I. Caretti, R. Torres and O. Sánchez, *J. Phys. D: Appl. Phys.*, 2012, **45**, 025303.

20 A. Steinfeld, A. Frei, P. Kuhn and D. Wuillemin, *Int. J. Hydrogen Energy*, 1995, **20**, 793–804.

21 L. Thum, M. Rudolph, R. Schomäcker, Y. Wang, A. Tarasov, A. Trunschke and R. Schlögl, *J. Phys. Chem. C*, 2019, **123**, 8018–8026.

22 A. Pöppl and G. Völkel, *Phys. Status Solidi A*, 1989, **115**, 247–255.

23 R. Chen, J. Wang, S. Luo, L. Xiang, W. Li and D. Xie, *Appl. Catal., B*, 2020, **264**, 118554.

24 X. Fu, J. Li, J. Long, C. Guo and J. Xiao, *ACS Catal.*, 2021, **11**, 12264–12273.

25 M. Zhang, F. Averseng, J.-M. Krafft, P. Borghetti, G. Costentin and S. Stankic, *J. Phys. Chem. C*, 2020, **124**, 12696–12704.

26 J. Qi and X. Hu, *Phys. Chem. Chem. Phys.*, 2020, **22**, 3953–3958.

27 R. H. Borgwardt, *Ind. Eng. Chem. Res.*, 1989, **28**, 493–500.

28 K. Fink, *Phys. Chem. Chem. Phys.*, 2006, **8**, 1482–1489.

29 G. Lassaletta, A. Fernández, J. P. Espinós and A. R. González-Elipe, *J. Phys. Chem.*, 1995, **99**, 1484–1490.

30 J. P. Espinós, J. Morales, A. Barranco, A. Caballero, J. P. Holgado and A. R. González-Elipe, *J. Phys. Chem. B*, 2002, **106**, 6921–6929.

31 G. S. Henderson, F. M. F. de Groot and B. J. A. Moulton, *Rev. Mineral. Geochem.*, 2014, **78**, 75–138.

32 Y. Hu, N. Wang and Z. Zhou, *Catal. Sci. Technol.*, 2021, **11**, 2518–2528.

33 A. Giehr, L. Maier, S. A. Schunk and O. Deutschmann, *ChemCatChem*, 2018, **10**, 751–757.

34 N. U. Zhanpeisov, G. M. Zhidomirov and M. Baerns, *J. Mol. Catal. A*, 1995, **99**, 35–39.

35 J. Gao, Z. Hou, H. Lou and X. Zheng, in *Fuel Cells: Technologies for Fuel Processing*, ed. D. Shekhawat, D. Berry and J. Spivey, Elsevier, Oxford, UK, 2011, pp. 191–221.

36 G. Kumar, S. L. J. Lau, M. D. Krcha and M. J. Janik, *ACS Catal.*, 2016, **6**, 1812–1821.

37 X. Jiang, B. M. Lis, S. C. Purdy, S. Paladugu, V. Fung, W. Quan, Z. Bao, W. Yang, Y. He, B. G. Sumpter, K. Page, I. E. Wachs and Z. Wu, *ACS Catal.*, 2022, **12**, 11239–11252.

38 R. Philipp and K. Fujimoto, *J. Phys. Chem.*, 1992, **96**, 9035–9038.

39 V. H. J. M. dos Santos, D. Pontin, G. G. D. Ponzi, A. S. G. e Stepanha, R. B. Martel, M. K. Schütz, S. M. O. Einloft and F. D. Vecchia, *Constr. Build. Mater.*, 2021, **313**, 125413.

40 A. C. Alba-Rubio, J. Santamaría-González, J. M. Mérida-Robles, R. Moreno-Tost, D. Martín-Alonso, A. Jiménez-López and P. Maireles-Torres, *Catal. Today*, 2010, **149**, 281–287.

41 L. Zhu, M. Cao, H. Zhou, N. Zhang, J. Zheng, Y. Li and B. H. Chen, *Catal. Lett.*, 2014, **144**, 1188–1196.

42 Y. Wang, Q. Zhuang, Y. Takahashi and Y. Ohtsuka, *Catal. Lett.*, 1998, **56**, 203–206.

43 T. Yabe, Y. Kamite, K. Sugiura, S. Ogo and Y. Sekine, *J. CO2 Util.*, 2017, **20**, 156–162.

44 H. V. Thang, G. Pacchioni, L. DeRita and P. Christopher, *J. Catal.*, 2018, **367**, 104–114.

45 H. Wang, R. Schmack, S. Sokolov, E. V. Kondratenko, A. Mazheika and R. Kraehnert, *ACS Catal.*, 2022, **12**, 9325–9338.

46 Z. Zhang, Y. Gong, J. Xu, Y. Zhang, Q. Xiao, R. Xi, X. Xu, X. Fang and X. Wang, *Catal. Today*, 2022, **400–401**, 73–81.

47 G. I. Siakavelas, N. D. Charisiou, A. AlKhoori, S. Gaber, V. Sebastian, S. J. Hinder, M. A. Baker, I. V. Yentekakis, K. Polychronopoulou and M. A. Goula, *Mol. Catal.*, 2022, **520**, 112157.

48 S. N. Bukhari, C. C. Chong, H. D. Setiabudi, N. Ainirazali, M. A. A. Aziz, A. A. Jalil and S. Y. Chin, *Int. J. Hydrogen Energy*, 2019, **44**, 7228–7240.

49 Q. Pan, J. Peng, T. Sun, S. Wang and S. Wang, *Catal. Commun.*, 2014, **45**, 74–78.

50 X. Gao, Z. Wang, Q. Huang, M. Jiang, S. Askari, N. Dewangan and S. Kawi, *Catal. Today*, 2022, **402**, 88–103.

9866 | *Phys. Chem. Chem. Phys.*, 2023, **25**, 9859–9867

This journal is © the Owner Societies 2023

51 L. Zhang, L. Li, J. Li, Y. Zhang and J. Hu, *Top. Catal.*, 2014, **57**, 619–626.

52 X. Li, D. Li, H. Tian, L. Zeng, Z.-J. Zhao and J. Gong, *Appl. Catal., B*, 2017, **202**, 683–694.

53 Y. Wang, Q. Zhao, Y. Wang, C. Hu and P. Da Costa, *Ind. Eng. Chem. Res.*, 2020, **59**, 11441–11452.

54 U. P and S. Darbha, *J. Chem. Sci.*, 2016, **128**, 957–965.

55 D. R. Burri, K.-M. Choi, D.-S. Han, Sujandi, N. Jiang, A. Burri and S.-E. Park, *Catal. Today*, 2008, **131** 173–178.

56 Istadi and N. A. S. Amin, *Fuel Process. Technol.*, 2006, **87**, 449–459.

This journal is © the Owner Societies 2023

Phys. Chem. Chem. Phys., 2023, **25**, 9859–9867 | **9867**